Seventh International Conference on Computational Fluid Dynamics (ICCFD7), Big Island, Hawaii, July 9-13, 2012

ICCFD7-2012-2204

Dissipation of upwind schemes at high wave numbers

V. Hannemann*, A. Siegmund**, K. Oßwald*, P. Birken**, K. Weinman*, A. Meister**
Corresponding author: Volker.Hannemann@DLR.de

* DLR - Institute of Aerodynamics and Flow Technology,
Bunsenstraße 10, 37073 Göttingen, Germany.
** Universität Kassel, Heinrich-Plett-Str. 40, 34132 Kassel, Germany.

Abstract: A modification of the Roe scheme aimed at low Mach number flows is discussed. It improves the dissipation of kinetic energy at the highest resolved wave numbers in a low Mach number test case of decaying isotropic turbulence. No conflict is observed between the reduced dissipation and the accuracy or stability of the scheme in any of the investigated test cases ranging from low Mach number potential flow to hypersonic viscous flow around a cylinder.

Keywords: Riemann Solvers, Upwind schemes, Dissipation.

1 Introduction

When approximate Riemann solvers were introduced into Godunov type schemes about three decades ago, an efficient way of simulating gas dynamic flows was found enabling to capture shocks within a few grid cells. In the following years many different approximate schemes were created and successfully improved to satisfy the entropy condition and handle the carbuncle phenomenon. Focusing on the schemes for perfect gas, the development of numerical flux functions was then dominated for many years by modifications to enable accurate results at low Mach numbers without loosing the stable and accurate resolution of high Mach number flow features. A particular solution to the accuracy problem at low Mach numbers for unsteady flow computations was found in the 1990s by Guillard and Viozat [1] using a preconditioning technique. However, this was subsequently shown to have stability problems [2, 3]. Therefore, different approaches have been taken in the last ten years.

As a second motivation, we consider time resolved high Mach number turbulent flow fields, computed via Large-Eddy Simulations (LES) or Detached Eddy Simulations (DES). This has been made possible due to the incresing computer power of recent years and exhibits a new challenge for upwind schemes. Excessive numerical dissipation in the range of higher resolved wave numbers prohibits the accurate resolution of the turbulent kinetic energy in that regime.

For the low Mach number problem, Thornber et. al. suggest a modification of the MUSCL reconstruction step [4], which changes the response of the flux function by reducing the velocity jump between the left and right states with decreasing Mach number. Beside a positive influence in the high wave number regime, it even improves the low Mach number ability of many Riemann solvers, as long as they are not already modified to resolve low Mach number flows. Combining it with low Mach number versions, the dissipation of the resulting scheme becomes too low. We investigate a different approach, based on the low Mach number modification of the Roe scheme proposed by Rieper [5]: reducing the dissipation within the Riemann solver in order to improve the solution for high wave numbers. Rieper modifies a formulation of the Roe scheme in which it is written as the central mean of the Euler fluxes plus dissipation terms. The dissipation associated with the difference in the normal velocity components is then reduced in the LMRoe scheme by multiplying the difference with the local Mach number in subsonic flows situations.

In this article, we consider an additional modification for the high wave number regime corresponding to a similar reduction on the differences of tangential velocity components on top of the normal components.

The following section describes the numerical flux function and the modifications investigated here. It is followed by some examples to demonstrate the range of applicability and culminates with the results in the case of decaying isotropic turbulence (DIT). The DIT test case offers a view on the numerical dissipation of the scheme with respect to the resolved wave numbers of the flow. All numerical results have been calculated with the DLR-TAU code - a second order finite volume method formulated on the dual grid of a conform mesh consisting of tetrahedra, prisms, pyramids and hexahedra. The Navier-Stokes equations are solved for a one component perfect gas with an additional sub-grid scale model in case of the DIT simulations. Although most of the presented results are achieved on structured grids the final focus of the investigation is to find an efficient and stable method to resolve large scale turbulent motion in hypersonic flow fields on generalized meshes. The reported success with the upwind scheme on structured grids is therefore only an important first step. In the last section before the conclusions some further ideas are discussed to identify the sources of the excessive numerical dissipation on the higher wave numbers in the framework of a second order finite volume upwind scheme.

Regarding notation, vectors in the coordinate space $\Re^3$ are underlined whereas bold faced variable names indicate vectors of the equation space.

2 Riemann solver

The numerical flux F_{LR} of the Roe-Pike method approximating the solution of the Riemann problem between the constant states L and R in case of the three dimensional Euler equations can be summarized as (see e.g. [6]):

$$\mathbf{F}_{LR} = \frac{1}{2}(\mathbf{F}_L + \mathbf{F}_R) - \frac{1}{2}\sum_{i=1}^{5} \alpha_i \, |\tilde{\lambda}_i| \, \mathbf{K}^i. \tag{1}$$

Here, the Euler flux $\mathbf{F}$ is evaluated in the direction of the unit normal vector $\underline{n}$ of the plane interface between L and R:

$$\mathbf{F} = \begin{bmatrix} \rho \, u_n \\ \rho \, u_n \, \underline{u} + p \, \underline{n} \\ \rho \, u_n \, H \end{bmatrix} \text{ with } u_n = \underline{u} \cdot \underline{n}$$

and the density ρ, velocity vector $\underline{u}$, pressure p and total enthalpy $H = h + 0.5 \, \underline{u} \cdot \underline{u}$. The wave strengths α_i, wave speeds or eigenvalues λ_i and eigenvectors $\mathbf{K}^i$ are given as:

$$\mathbf{K}^1 = \begin{bmatrix} 1 \\ \tilde{\underline{u}} - \tilde{a} \, \underline{n} \\ \tilde{H} - \tilde{a} \, \tilde{u}_n \end{bmatrix} ; \; \mathbf{K}^2 = \begin{bmatrix} 1 \\ \tilde{\underline{u}} \\ 0.5 \, \tilde{\underline{u}} \cdot \tilde{\underline{u}} \end{bmatrix} ; \; \mathbf{K}^3 = \begin{bmatrix} 0 \\ \underline{t}_1 \\ \tilde{u}_{t_1} \end{bmatrix} ; \; \mathbf{K}^4 = \begin{bmatrix} 0 \\ \underline{t}_2 \\ \tilde{u}_{t_2} \end{bmatrix} ; \; \mathbf{K}^5 = \begin{bmatrix} 1 \\ \tilde{\underline{u}} + \tilde{a} \, \underline{n} \\ \tilde{H} + \tilde{a} \, \tilde{u}_n \end{bmatrix},$$

$$\tilde{\lambda}_1 = \tilde{u}_n - \tilde{a} \quad ; \quad \tilde{\lambda}_2 = \tilde{u}_n \quad ; \quad \tilde{\lambda}_3 = \tilde{u}_n \quad ; \quad \tilde{\lambda}_4 = \tilde{u}_n \quad ; \quad \tilde{\lambda}_5 = \tilde{u}_n + \tilde{a} \, ,$$

$$\alpha_1 = \frac{\delta p - \tilde{\rho} \, \tilde{a} \, \delta u_n}{\tilde{a}^2} \quad ; \quad \alpha_2 = \delta \rho - \frac{\delta p}{\tilde{a}^2} \quad ; \quad \alpha_3 = \tilde{\rho} \, \delta u_{t_1} \quad ; \quad \alpha_4 = \tilde{\rho} \, \delta u_{t_2} \quad ; \quad \alpha_5 = \frac{\delta p + \tilde{\rho} \, \tilde{a} \, \delta u_n}{2\tilde{a}^2}.$$

Herein a denotes the speed of sound and $\underline{t}_1$ and $\underline{t}_2$ arbitrary orthogonal unit tangential vectors spanning the plane with the normal $\underline{n}$. The velocity components in the tangential directions are $u_{t_1} = \underline{u} \, \underline{t}_1$ and $u_{t_2} = \underline{u} \, \underline{t}_2$. δ and $\tilde{}$ indicate the difference between the right and left states (e.g. $\delta p = p_R - p_L$) and respectively the Roe averages given by:

$$\tilde{\rho} = \sqrt{\rho_L \, \rho_R} \; ; \; \tilde{\underline{u}} = \frac{\sqrt{\rho_L} \, \underline{u}_L + \sqrt{\rho_R} \, \underline{u}_R}{\sqrt{\rho_L} + \sqrt{\rho_R}} \; ; \; \tilde{H} = \frac{\sqrt{\rho_L} \, H_L + \sqrt{\rho_R} \, H_R}{\sqrt{\rho_L} + \sqrt{\rho_R}} \; ; \; \tilde{a} = \sqrt{(\gamma - 1)(\tilde{H} - 0.5 \, \tilde{\underline{u}} \cdot \tilde{\underline{u}})}.$$

The entropy fix according to van Leer is applied on the acoustic waves ($k = 1$ and $k = 5$):

$$|\tilde{\lambda}_k|^* = \begin{cases} |\tilde{\lambda}_k| & , |\tilde{\lambda}_k| \geq 2\,\delta\hat{\lambda}_k \\ \frac{\tilde{\lambda}_k^2}{4\,\delta\hat{\lambda}_k} + \delta\hat{\lambda}_k & , |\tilde{\lambda}_k| < 2\,\delta\hat{\lambda}_k \end{cases} \quad \text{with } \delta\hat{\lambda}_k = \max(\lambda_k^R - \lambda_k^L, 0).$$

In order to avoid shock instabilities (carbuncle phenomenon) the shock indicator proposed in [7] for the AUSMDV switch is used to locally modify the wave speed λ_2 according to Liou [8]:

$$|\tilde{\lambda}_2|^* = \begin{cases} |\tilde{\lambda}_2| & , ssw_L = ssw_R = 0 \\ \max(\tilde{a}, |\underline{\tilde{u}}|) & , \text{else} \end{cases}$$

with

$$ssw_i = \begin{cases} 1\ , \lambda_1^i > 0 \text{ and } \lambda_1^j < 0 & \text{for any neighbor j of i} \\ 1\ , \lambda_5^i > 0 \text{ and } \lambda_5^j < 0 & \text{and respective normal } \underline{n}_{ij} \\ 0\ , \text{else.} & \end{cases}$$

2.1 Modification according to Thornber et al.

Thornber et al. modify the left and right velocities in a subsonic situation linear with the Mach number in order to reach the arithmetic mean of the velocities at Mach number $M = 0$:

$$\begin{aligned} \underline{u}_L^* &= \frac{(1+z)\,\underline{u}_L + (1-z)\,\underline{u}_R}{2} \\ \underline{u}_R^* &= \frac{(1+z)\,\underline{u}_R + (1-z)\,\underline{u}_L}{2} \end{aligned} \qquad \text{with } z = \min\left(1, \max(M_L, M_R)\right) \text{ and } M = \frac{|\underline{u}|}{a} \quad . \tag{2}$$

The Mach numbers used are the real flow Mach numbers independent of the normal direction in which the flux is evaluated. The primary effect of the modification in case of the Roe-Pike method is the linear reduction of Δu_n, Δu_{t_1} and Δu_{t_2} with decreasing Mach number and the respective influence on the wave strengths. Secondary effects are due to the non linear terms in the Euler flux evaluation and the difference between the arithmetic mean and the Roe averaged velocities.

2.2 LMRoe and beyond

The LMRoe scheme of Rieper [5] is a simple modification of the Roe-Pike scheme to achieve a low Mach number variant. The same linear blending function z as given in equation (2) is applied within the approximate Riemann solver only on δu_n which effects the wave strengths of the acoustic waves α_1 and α_5.

$$(\delta u_n)^* = z\,\delta u_n$$

The reduction of the numerical dissipation depending on the jump in the normal component of the velocities is sufficient to improve the behavior of the scheme at low Mach numbers. In the vicinity of shocks small disturbances are observed which are avoided by using the shock indicator to keep the original scheme unmodified there:

$$(\delta u_n)^* = \begin{cases} z\,\delta u_n & , ssw_L = ssw_R = 0 \\ \delta u_n & , \text{else} \end{cases} \quad .$$

Applied in the test case of decaying isotropic turbulence (DIT) it is shown in section 4 that the dissipation of the scheme in the higher wave number regime is too high to properly resolve the kinetic energy of the turbulent fluctuations.

The motivation for the following modifications are the knowledge of the success of the Thornber modification for all wave numbers in the DIT case and the question why the tangential components of the velocity should need more numerical dissipation than the normal component. The first step in reducing the numerical dissipation associated with $\mathbf{K}^3$ and $\mathbf{K}^4$ is to apply the similar modification for both tangential components t_1 and t_2:

$$(\delta u_t)^* = \begin{cases} z\,\delta u_t & , ssw_L = ssw_R = 0 \\ \delta u_t & , \text{else} \end{cases} \quad .$$

The dependence of the dissipation on the flow Mach number is well motivated via asymptotic analysis for the low Mach number extension applied on Δu_n. In case of the high wave number dissipation of the kinetic energy a similar theoretical argument is missing. Therefore, the search for an optimal dissipation depends on heuristics. The second step is to modify the weighting function z to be used on the tangential components:

$$(\delta u_t)^* = \begin{cases} z^*\,\delta u_t \;, ssw_L = ssw_R = 0 \\ \delta u_t \quad\;\; , \text{else} \end{cases}$$

$$z^* = \min\left(1, \max(M_L^n, M_R^n)\right) \quad \text{and } M^n = \frac{|u_n|}{a}.$$

The last modification makes the scheme less dissipative because z^* is always smaller or equal to z and will influence the dissipation even for supersonic flows.

3 Application of the low dissipation version of the Roe scheme

Several test cases have been conducted with the present modifications with a linear reconstruction of the primitive variables. The results of the current scheme are equal or better than the results reported in [5] for the LMRoe. Two cylinder test cases - a laminar supersonic flow field with heat transfer and a low Mach number inviscid flow field - are provided to demonstrate the investigated range of applications. A total variation diminishing (TVD) limiter is applied in case of the supersonic cylinder test. No TVD limiters are necessary in the low Mach number cases of the potential flow and of the DIT in the following section.

3.1 Supersonic cylinder

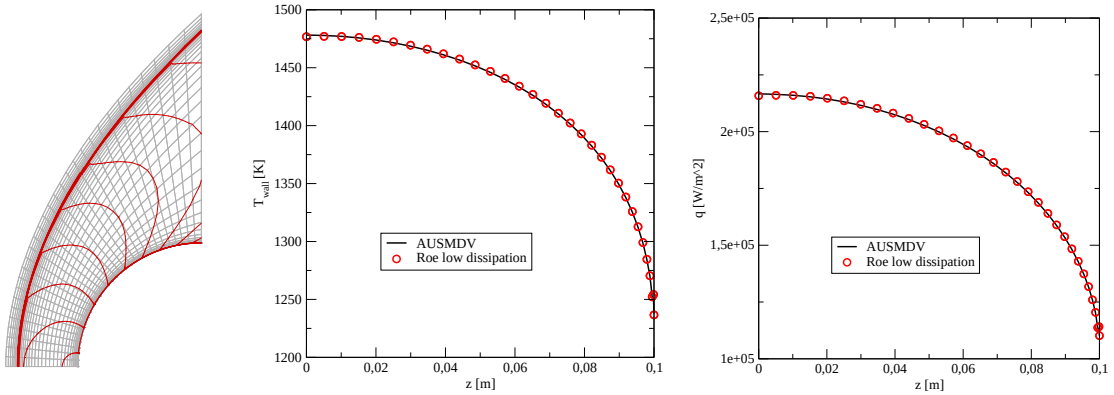

Figure 1: Mach 5 cylinder flow with radiative equilibrium at the wall; grid and Mach number isolines (left); wall temperature profile (middle) and heat flux profile (right) over the vertical coordinate z

The cylinder faces a Mach five flow of air ($\gamma = 1.4, R = 287\,J/(kg\,K)$) at normal conditions ($p_\infty = 101325Pa, T_\infty = 273.15K$). The related Reynolds number with respect to the radius of $0.1m$ is about 12.5 million. The temperature dependence of the viscosity is modeled via the Sutherland formula for air:

$$\mu(T) = 17.2 \cdot 10^{-6}\,Pa\,s \left(\frac{T}{T_\infty}\right)^{\frac{3}{2}} \frac{T_\infty + 110.33\,K}{T + 110.33\,K}.$$

The heat flux $\dot{q}$ to the wall is assumed to be equal to the heat flux radiated from the wall with an emissivity

$\epsilon = 0.8$ according to the Stefan-Maxwell law:

$$\dot{q} = \epsilon\,\sigma\,T_{wall}^4 \qquad \text{with } \sigma = 56.7032 \cdot 10^{-9}\,\frac{W}{m^2\,K^4}.$$

The stable shock capturing and the accurate calculation of the wall temperature together with the related wall heat flux are depicted in Figure 1. A good agreement is shown with results calculated with the AUSMDV.

3.2 Potential flow

The Euler equations are solved to simulate the inviscid flow field around a cylinder at a Mach number of $M_\infty = 0.001$ characterizing the relative motion of the fluid in the farfield and the obstacle. The farfield boundaries are taken about 1000 cylinder diameters away from the surface. The solution shown in Figure 2 highlight the low Mach number capability of the modified scheme. At such low Mach numbers the unmodified Roe scheme does not provide a physical solution. Notice that the benefit of the modifications is restricted to the accuracy of the converged solution and do not improve the convergence behavior of the scheme on the way to a steady state solution.

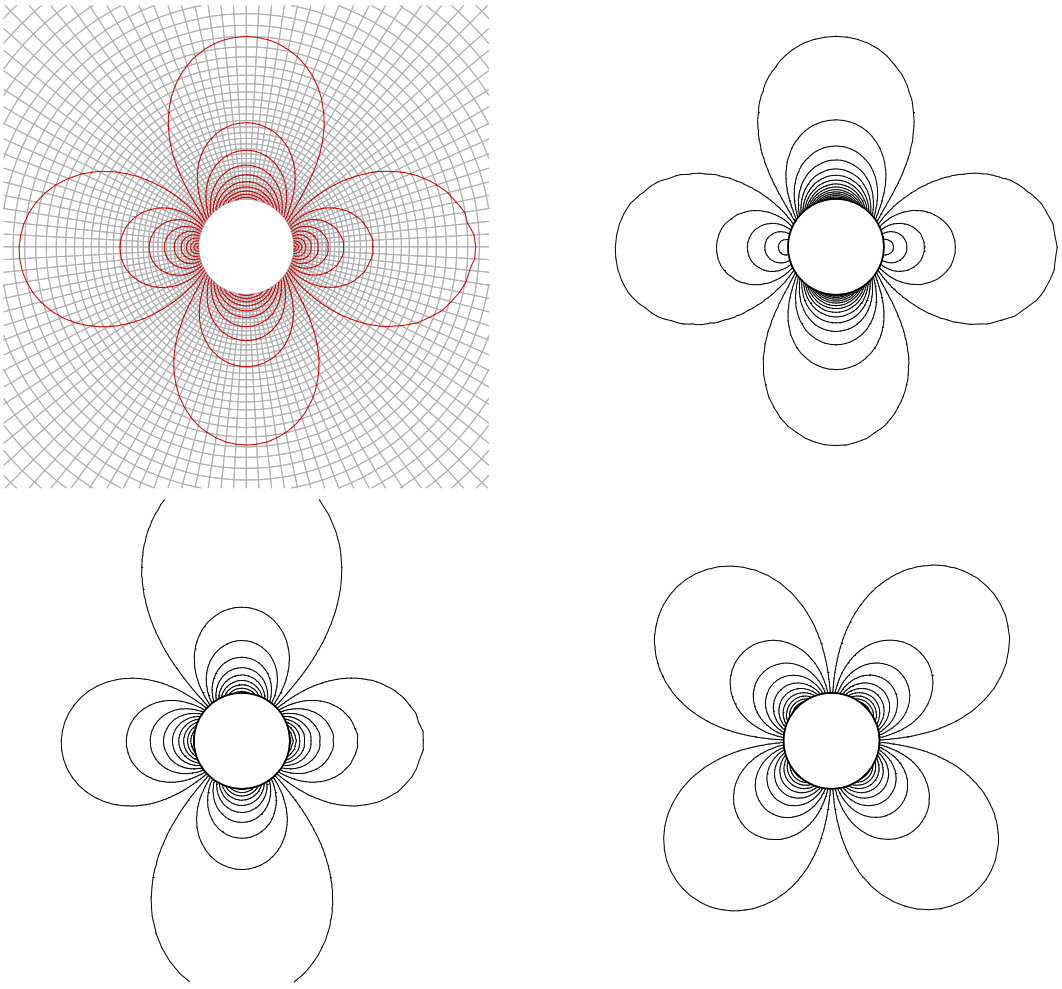

Figure 2: Inviscid flow field around a cylinder in a $M_\infty = 0.001$ flow coming from the left; grid detail and Mach number isolines (upper left); pressure isolines (upper right); horizontal velocity component (lower left); vertical velocity component (lower right)

4 Decay of isotropic turbulence (DIT)

Decaying isotropic turbulence is investigated on an equidistant Cartesian grid. The boundary conditions are chosen to be periodic in one coordinate direction and symmetric in the other directions. Earlier tests conducted during the DESider project [9] suggest**ed** that the evolution of second order statistical moments and spectra **are is** not influenced significantly by this choice of boundary condition as opposed to periodic boundaries on all computational domain boundaries. Note that the application of fully periodic boundaries using a dual-cell unstructured grid metric is non-trivial and has not yet been implemented in our code. A second order reconstruction of the primitive variables is used without limiters due to the continuous flow field at the low Mach numbers ($M_{\max} < 0.016$).

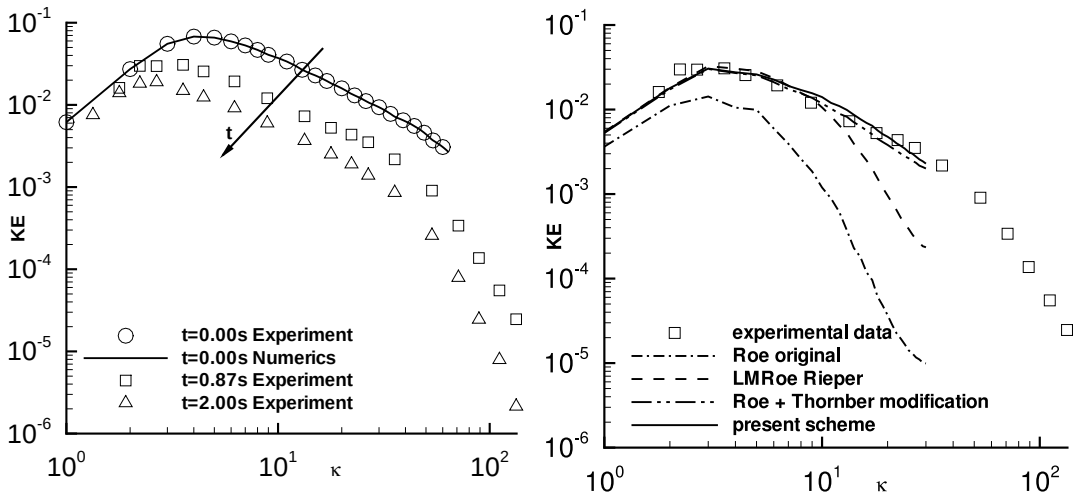

Figure 3: Turbulent kinetic energy spectra (left) at t=0s, t=0.87s and t=2s in the case of decaying isotropic turbulence; experimental data taken from Comte-Bellot and Corrsin [10]; numerical spectra at t=0.87s on a 64^3 hexahedral grid (right)

The initial velocity field $u(x, t = 0)$ is divergence free and is constructed in order to replicate the experimental kinetic energy spectra [10] over all resolvable wave numbers. The spectra measured in the Comte-Bellot and Corrsin experiment, as shown in Figure 3 on the left, are used as a measure to evaluate the flow solutions obtained using various numerical schemes. Note that a typical energy spectrum can be characterized by a power-law form $E(k) = C\,k^p$ where $p \approx 2 - 4$ in the energy-containing range, $p \approx -5/3$ in the inertial subrange and with a final range of decaying turbulence [11]. The numerical simulation should return a resolved inertial range so that the transfer of energy from large scales to smaller scales is adequately modeled within the context of LES and hybrid RANS/LES simulations. The energy transfer process is strongly dependent on the total dissipation of the numerical scheme, which can be argued to consist of three major contributions:

1. sub-grid scale (SGS) stresses,
2. molecular viscosity, and
3. the numerical dissipation of the scheme.

For the work discussed in this paper contributions due to transport of molecular viscosity are small and the SGS model coefficient calibration has been undertaken using a central scheme with matrix dissipation. The Spalart-Allmaras turbulence model [12] provides our SGS model within the context of Detached Eddy Simulation [13, 14, 15]. Note that the focus of the current work is in determining the characteristics of the modified Roe scheme, so that both SGS model and molecular viscosity are kept constant throughout

the investigation. The numerical dissipation of the unmodifed schemes in the high wave number regimes discussed in the paper is sufficiently strong enough to dominate over viscous and SGS effects. On a 64^3 hexahedral grid wave numbers up to 31 should be resolved. In Figure 3 on the right the results at $t = 0.87s$ of the second order upwind scheme are shown for various flux functions. The significantly dissipative result of the original Roe scheme is representative for most standard approximate Riemann solvers e.g. AUSMDV. The improved performance of the LMRoe scheme is typical for low Mach number enhanced versions like the AUSM+up. The original scheme with the modification in the reconstructed velocities according to Thornber et al. and the low dissipation version presented here are both resolving the energy cascade over all wave numbers on this grid.

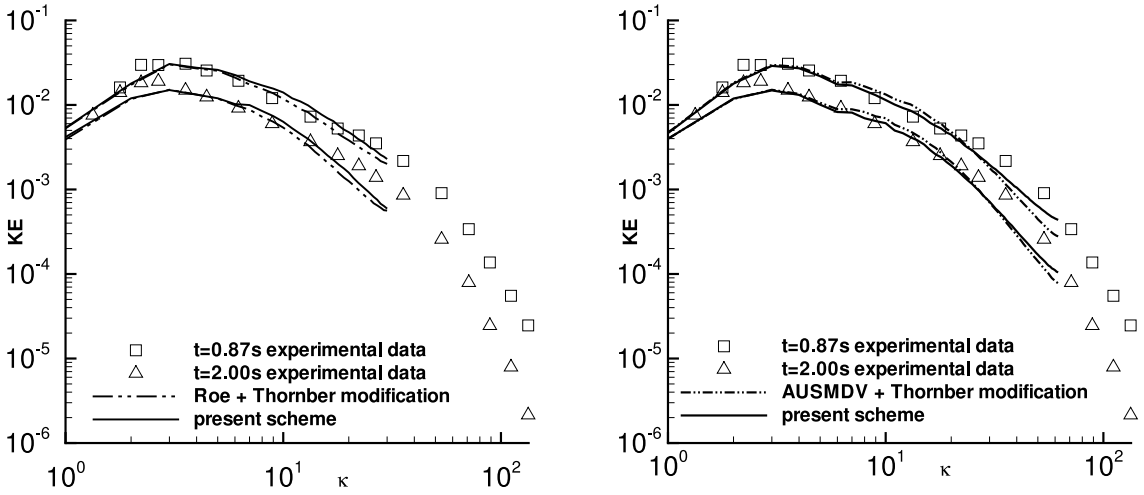

Figure 4: Turbulent kinetic energy spectra at t=0.87s and t=2s in the case of decaying isotropic turbulence on a 64^3 (left) and 128^3 (right) hexahedral grid; experimental data taken from Comte-Bellot and Corrsin [10]

The results at time $t = 2s$ are given in Figure 4 on the left for the two schemes appropriate to this test case. Both show a reasonable good agreement with the experimental data. Although the formulations of both schemes are quite close, the proposed modification within the Roe scheme seems to be a little less dissipative in the high wave number regime than the Thornber modification with the original scheme.

The results of the present scheme on a finer mesh 128^3 are shown in Figure 4 on the right. The improved resolution at higher wave numbers confirms the promising numerical dissipation properties of the scheme within the framework of LES or DES. In addition results achieved with the Thornber modification together with an AUSMDV scheme underline the general applicability of the modification given in equation 2. Again the modified Roe scheme shows less dissipative results at the highest resolved wave numbers.

The same 128^3 nodes as before are reconnected with tetrahedral instead of hexahedral elements. The change in the grid topology allows the numerical dissipation in the higher resolved wave number range to grow again as can be seen in Figure 5 on the left hand side. Although the results offer an improvement over those returned without the modifications, the value of p returned in the inertial interval is significantly less than $-5/3$, implying an unphysically high dissipation of energy.

The rotational and translational symmetry of the two grids are different. The tranlational offset for example is twice as large in the tetrahedral mesh compared to the hexahedral mesh. But this symmetry aspect should not deteriorate the numerical dissipation of the scheme in the higher resolved wave number range because simulations using the central scheme with matrix dissipation show similar good results on both discretizations, as can be seen on the right hand side of Figure 5.

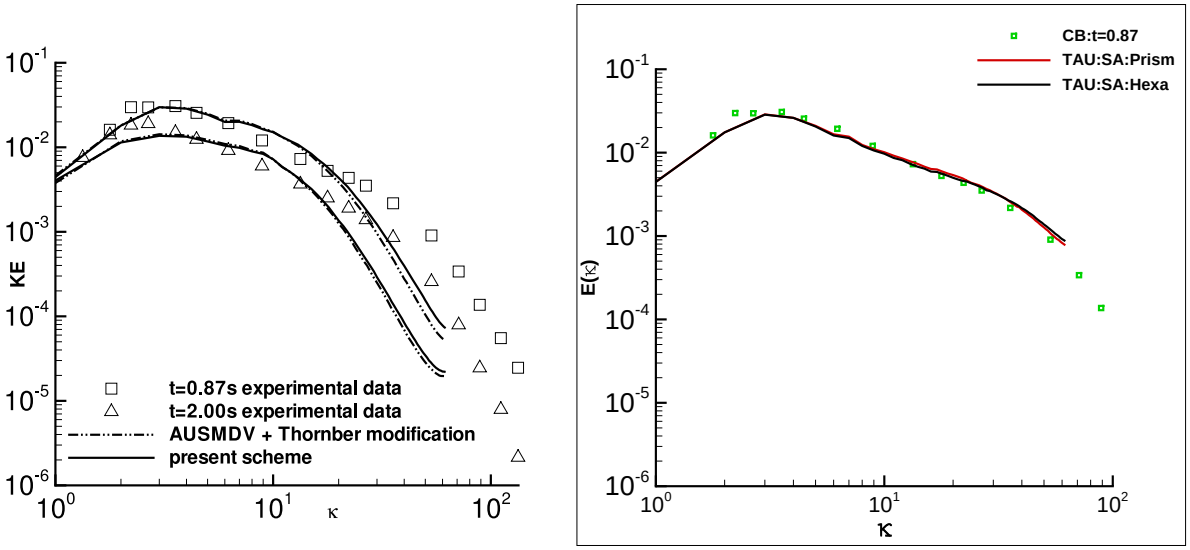

Figure 5: Turbulent kinetic energy spectra at t=0.87s and t=2s in the case of decaying isotropic turbulence on a 128^3 tetrahedral grid (left); experimental data taken from Comte-Bellot and Corrsin [10]; results at t=0.87s of the central scheme with matrix dissipation (right) on hexahedral and prismatic grid

5 Further sources of dissipation in the finite volume scheme

In the preceding sections the focus of the investigation is on the numerical flux function whereas here the other parts of our method are discussed with respect to accuracy issues. Assuming a exact flux is integrated over the volume's surface, a correct residual is then achieved at time t for each balance equation. The next steps within our finite volume method before applying again the numerical flux function are:

- **The time integration** determines the update of the cell averages of the conservative variables to reach the next time level $t + \Delta t$. Usually, the time integration has a dissipative influence on the method, but this is not investigated here further, because the same time integration (explicit two stage Runge Kutta, formally of second order in Δt) is used in all calculations.

- **The calculation of the primitive variables and their gradients** is usually split into two independent steps. First in each cell primitive variables are computed from the conservative variables. Secondly, the values of the primitive variables are assumed to be located at a specific point within each volume and the gradients $\underline{\nabla}$ are calculated based on the relative positions of the located values in neighboring cells. The barycenter of each volume is the only second order accurate choice to locate a cell averaged mean value point wise. Nevertheless, taking piecewise linear distributions of the primitive variables to represent the solution on each volume V, performing the both steps independently introduces a second order error, e.g. in one dimensional space:

$$\overline{\rho u} = \frac{1}{V}\int_V \rho\, u\, dV = \frac{1}{V}\int_V (\bar{\rho} + \nabla\rho\,\Delta x)\,(\bar{u} + \nabla u\,\Delta x)\, dV$$

$$= \bar{\rho}\,\bar{u} + (\bar{\rho}\,\nabla u + \bar{u}\,\nabla\rho)\,\frac{1}{V}\int_V \Delta x\, dV + \nabla\rho\,\nabla u\,\frac{1}{V}\int_V \Delta x\,\Delta x\, dV$$

with $\Delta x = x - \bar{x}$ and the cell averaged momentum $\overline{\rho u}$. If the reconstruction point $\bar{x}$ within the cell is the barycenter of the volume, the second integral vanishes ($\int_V \Delta x\, dV \equiv 0$) and consequently one

obtains:

$$\overline{\rho u} = \bar{\rho}\,\bar{u} + \nabla\rho\,\nabla u \underbrace{\frac{1}{V}\int_V \Delta x\,\Delta x\,dV}_{=:\,Ix^2} \ .$$

The remaining, purely geometry dependent term Ix^2 is of second order $O(h^2)$ and therefore usually ignored in the context of a second order scheme. But within the same order of approximation it could be seen as a condition under which the gradients have to be calculated. It could as well be seen as a correction to get an appropriate mean value $\bar{u}$:

$$\bar{u} = \frac{\overline{\rho u} - \nabla\rho\,\nabla u\,Ix^2}{\bar{\rho}} \ .$$

Across discontinuities in f the difference quotient $\frac{\delta f}{\delta x}$ goes to infinity when the jump δf stays constant and δx is going to zero. This makes the Ix^2 containing term of order one or zero depending whether the flow is discontinuous in only one or both variables (ρ and u). Nevertheless, this step is not further investigated here because the focus is on the resolution of smooth flows like in the DIT test case and the same splitting is used with the central scheme.

- **The reconstruction step** of the second order upwind scheme leads to a significant difference compared to a central scheme although the numerical flux function in equation (1) looks like a central formulation plus an artificial dissipation term. An approximate Riemann solver only gets two constant states as an input and the numerical dissipation terms in equation (1) are calculated based on this information. By contrast, the dissipation calculation in a central scheme uses a much wider stencil of information from all directions. This difference culminates in the case when the left and right reconstructed states are the same and any consistent numerical flux function has to reproduce the exact Euler flux of this state without introducing any numerical dissipation. Therefore, the smaller the differences of the reconstructed variables are, the smaller becomes the influence of the numerical flux function on the dissipation of the scheme. In smooth flow regions the linear (or in other schemes higher order) reconstruction including the non linear limiters becomes an important part of the scheme for the accuracy of the solution and the numerical dissipation of the scheme.

Having achieved reasonable results for the DIT case on hexahedral grids with the proposed upwind method, the following section focuses on modifications of the reconstruction procedure. During the reconstruction more information is available than inside the approximate Riemann solver. Although additional preprocessed information can be useful inside the numerical flux function, like the shock switch sensor mentioned above, the first ideas reported here modify the reconstructed states and leave the flux function unchanged.

5.1 Entropy and specific enthalpy limits for the reconstruction

The typical reconstruction of the variables is motivated and derived for scalar equations. The procedure of gradient and limiter computation is independently applied to each component of the reconstructed vector of the primitive variables. To investigate if this is justified, we take a look at the dependence of the enthalpy h and the function $s = \exp(\frac{\hat{s}-const}{c_V})$ of the entropy $\hat{s}$ (with the specific heat at constant volume c_V) on the reconstructed primitive variables for a perfect gas with an adiabatic exponent γ:

$$s = \frac{p}{\rho^\gamma} \qquad \text{and} \qquad h = \frac{\gamma}{\gamma-1}\frac{p}{\rho}.$$

Defining the reconstruction part $\Delta v = v - v_0$ as the difference between the reconstructed value v and the cell averaged value v_0, it follows:

$$\frac{s-s_0}{s_0} = \frac{\frac{p_0+\Delta p}{(\rho_0+\Delta\rho)^\gamma} - \frac{p_0}{\rho_0^\gamma}}{\frac{p_0}{\rho_0^\gamma}} \qquad \text{and} \qquad \frac{h-h_0}{h_0} = \frac{\frac{p_0+\Delta p}{\rho_0+\Delta\rho} - \frac{p_0}{\rho_0}}{\frac{p_0}{\rho_0}}$$

$$\frac{\Delta s}{s_0} = \frac{1+\frac{\Delta p}{p_0}}{\left(1+\frac{\Delta \rho}{\rho_0}\right)^{\gamma}} - 1 \qquad \text{and} \qquad \frac{\Delta h}{h_0} = \frac{1+\frac{\Delta p}{p_0}}{1+\frac{\Delta \rho}{\rho_0}} - 1 \,.$$

The normalized relation between Δp and $\Delta \rho$ at an evaluation point 0 is given by:

$$\frac{\Delta p}{p_0} = \left(1+\frac{\Delta s}{s_0}\right)\left(1+\frac{\Delta \rho}{\rho_0}\right)^{\gamma} - 1 \qquad \text{and} \qquad \frac{\Delta p}{p_0} = \left(1+\frac{\Delta h}{h_0}\right)\left(1+\frac{\Delta \rho}{\rho_0}\right) - 1 \,.$$

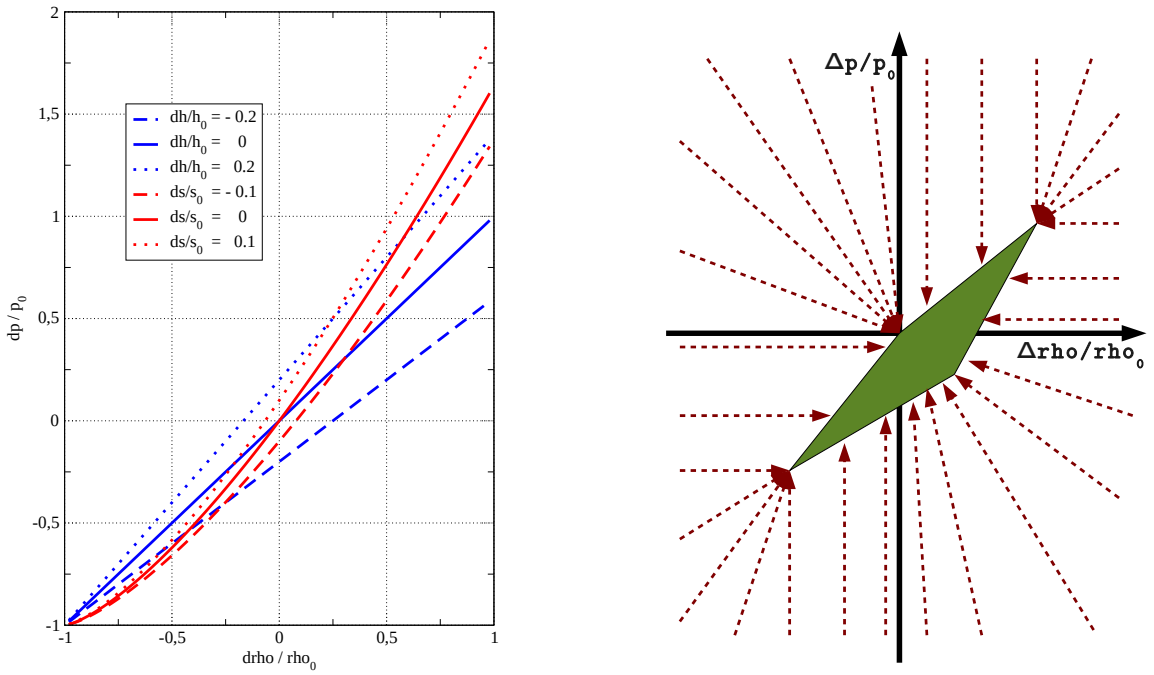

Figure 6: Left: normalized dependency of $\Delta p = f(\Delta \rho)$; right: sketch of the projection directions towards the allowed region

The relations are shown on the left hand side of Figure 6 for some arbitrary large values of $\frac{\Delta s}{s_0}$ and $\frac{\Delta h}{h_0}$ to enhance the visibility. The evaluation point is at $(0;0)$ equal to the first order reconstruction with $\Delta p = \Delta \rho = 0$. Values below -1 on both axis are meaningless due the positivity of pressure and density. The curved isolines for the entropy difference to the reference point entropy as well as the straight lines of constant enthalpy difference to the reference point enthalpy do all meet at $(-1;-1)$ equivalent to zero pressure and zero density. If an interval of valid entropy or enthalpy difference to the reference state can be defined then the variation of density and pressure is only independent within these limits.

The choice of limits investigated here takes only the left and right cell averages in addition to the reconstructed states, keeping the modification of the reconstruction process as local as possible. The allowed interval of the entropy function is set to half of the difference between the left and right cell averages in order to avoid reconstructed states with extrapolated entropy or in other words to ensure a monotone distribution of entropy between the two cell averages. For an isentropic flow field the allowed region degenerates to one line which happens for most low Mach number flows without viscous effects. Similar limits are taken for the

total enthalpy H, which let the velocities enter the considerations:

$$H = h + 0.5\,\underline{u}\cdot\underline{u} \qquad \Rightarrow \qquad \Delta H = \Delta h + 0.5\,\left[(\underline{u}_0 + \underline{\Delta u})\cdot(\underline{u}_0 + \underline{\Delta u}) - \underline{u}_0\cdot\underline{u}_0\right]$$

$$\Delta h = \Delta H - u_0\,\Delta u\,\cos(\alpha) - 0.5\,(\Delta u)^2 \qquad \text{with } u_0 = |\underline{u}_0|,\ \Delta u = |\underline{\Delta u}|,\ \cos(\alpha) = \frac{\underline{u}_0\cdot\underline{\Delta u}}{u_0\,\Delta u} \tag{3}$$

The limits for the enthalpy are set to the extreme when evaluating equation (3) with Δu either being zero or the Δu of the local reconstruction.

Depending on the limits for Δs and Δh the intersection of the two isentropes (0 and Δs) and the two constant enthalpy lines (0 and Δh) defines a region within which the normalized pressure and density differences can vary independently. Although the precise position of the region depends on the signs of Δs and Δh some general remarks can be stated:

- the origin $(0;0)$ is always part of the region and therefore in each quadrant exists at least one point of the allowed region,
- the point of the region with the maximal value of $\Delta\rho$ is unique and represents at the same time the maximal value of Δp,
- the point of the region with the minimal value of $\Delta\rho$ is unique and represents at the same time the minimal value of Δp.

If the reconstruction lies outside this region an additional limitation ($0 \le \lambda \le 1$) is applied to one or the other or both reconstructed variables in order to bring the reconstructed values to the boundaries of that region. The procedure is sketched in Figure 6 on the right. Within the green area the reconstruction stays untouched, whereas a reconstructed value outside is projected along the red dashed arrows onto the boundary of the green region.

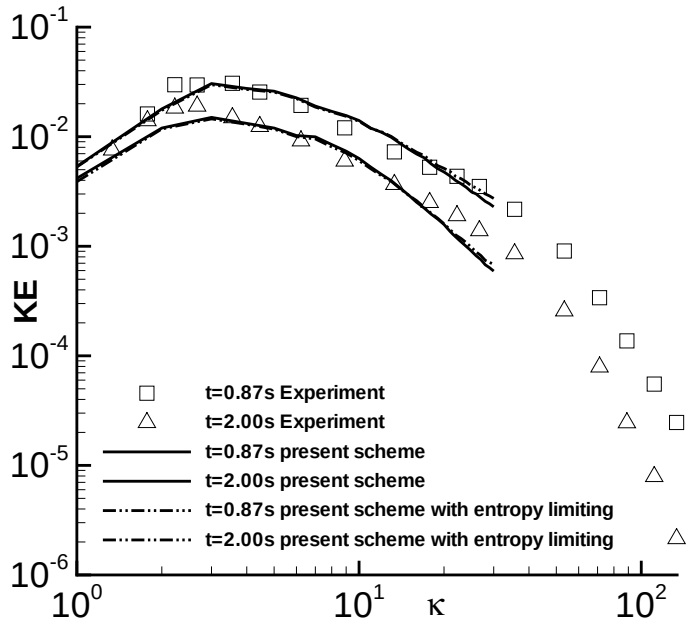

Figure 7: Turbulent kinetic energy spectra at t=0.87s and t=2s in the case of decaying isotropic turbulence on a 64^3 hexahedral grid; experimental data taken from Comte-Bellot and Corrsin [10]

The influence of this limitation in case of the DIT test on a hexahedral mesh is shown in Figure 7. A little less dissipation at the highest wave numbers can be observed. Unfortunately, the results on the tetrahedral grid (not shown) stay unchanged. Nevertheless, an influence of the reconstruction step on the dissipation at high wave numbers is shown. Other, less restrictive ways than the limitation described above, as well as modifications of the reconstructed velocities will be investigated in the future in order to achieve a further improvement of the scheme on tetrahedral grids.

6 Conclusion

The low dissipation version of the Roe-Pike scheme is applicable without user defined changes for a large Mach number regime. Improved results are achieved on hexahedral meshes in case of the decaying isotropic turbulence. An influence of the reconstruction step on the dissipation at high wave numbers is shown by a modified reconstruction, which reduces the density and pressure reconstruction with respect to entropy and enthalpy constrains.

The total Mach number in the DIT test case is below 0.016 thus switching the z weighted terms almost completely off. Therefore, the benefit or failure of the switching function z in the low dissipation Roe scheme has to be tested in future at different higher Mach numbers between 0.1 and 0.9. The additional dissipation showing up at high wave numbers on the tetrahedral mesh is not understood so far and will be investigated further.

Acknowledgement

Financial support has been provided by the German Research Foundation (Deutsche Forschungsgemeinschaft – DFG) in the framework of the Sonderforschungsbereich Transregio 30, project C2, as well as in the framework of the Sonderforschungsbereich Transregio 40, project B5.

References

[1] H. Guillard and C. Viozat. On the Behaviour of Upwind Schemes in the Low Mach Number Limit. *Computers & Fluids*, 28:63–86, 1999.

[2] P. Birken and A. Meister. Stability of Preconditioned Finite Volume Schemes at Low Mach Numbers. *BIT*, 45(3), 2005.

[3] S. Dellacherie. Analysis of Godunov type schemes applied to the compressible Euler system at low Mach number. *J. Comp. Phys.*, 229(4):978–1016, 2010.

[4] B. Thornber, A. Mosedale, D. Drikakis, D. Youngs, and R.J.R. Williams. An improved reconstruction method for compressible flows with low Mach number features. *Journal of Computational Physics*, 227:4873–4894, 2008.

[5] F. Rieper. A low-Mach number fix for Roe's approximate Riemann solver. *Journal of Computational Physics*, 230:5263–5287, 2011.

[6] E.F. Toro. *Riemann Solvers and Numerical Methods for Fluid Dynamics*. Springer, 1997.

[7] Y. Wada and M.-S. Liou. A Flux Splitting Scheme With High-Resolution and Robustness for Discontinuities. AIAA-94-0083, NASA Technical Memorandum 106452, 1994.

[8] M.-S. Liou. Mass Flux Schemes and Connection to Shock Instability. *Journal of Computational Physics*, 160:623–648, 2000.

[9] W. Haase, M. Braza, and A. Revell (Eds. DESider - A European Effort on Hybrid RANS-LES Modelling, Results of the European-Union Funded Project, 2004-2007. Series: Notes on Numerical Fluid Mechanics and Multidisciplinary Design, Vol. 103, 2009.

[10] G. Comte-Bellot and S. Corrsin. Simple Eulerian time correlation of full- and narrow-band velocity signals in grid generated, „isotropic“ turbulence. *Journal of Fluid Mechanics*, 48:273–337, 1971.

[11] W.K. George. The decay of homogeneous isotropic turbulence. *Phys. Fluids A*, 4(7):1492–1509, 1992.

[12] P.R. Spalart and S.R. Allmaras. A one-equation turbulence model for aerodynamic flows. Recherche A'erospatiale 1, 1994.

[13] P.R. Spalart, W.-H. Jou, M. Strelets, and S.R. Allmaras. Comments on the Feasibility of LES for Wings and on the Hybrid RANS/LES Approach. Advances in DNS/LES, Proceedings of the First AFOSR International Conference on DNS/LES, 1997.

[14] M. Strelets. Detached Eddy Simulation of Massively Separated Flows. AIAA Paper 2001–0879, 2001.

[15] M.L. Shur, P.R. Spalart, M. Strelets, and A.K. Travin. A hybrid RANS-LES approach with delayed-DES and wall-modelled LES capabilities. *International Journal of Heat and Fluid Flow*, 29:1638–1649, 2008.